Combined numerical and experimental investigation of the cavitation erosion process

Wang Jian
Research Center of Fluid Machinery Engineering and Technology, Jiangsu University, Zhenjiang 202013, China
Email: kin.jian.wang@gmail.com

Martin Petkovšek
Laboratory for Water and Turbine Machines, University of Ljubljana, Askerceva 6, 1000 Ljubljana, Slovenia
Email: martin.petkovsek@fs.uni-lj.si

Liu Houlin
Research Center of Fluid Machinery Engineering and Technology, Jiangsu University, Zhenjiang 202013, China
Email: liuhoulin@ujs.edu.cn

Brane Širok.
Laboratory for Water and Turbine Machines, University of Ljubljana, Askerceva 6, 1000 Ljubljana, Slovenia
Email: brane.sirok@fs.uni-lj.si

Matevž Dular (corresponding author)
Laboratory for Water and Turbine Machines, University of Ljubljana, Askerceva 6, 1000 Ljubljana, Slovenia
Email: matevz.dular@fs.uni-lj.si
Phone: +386 31 203044
Fax: +386 1 2518567

ABSTRACT

We are comparing results of numerical simulations against high speed simultaneous observations of cavitation and cavitation erosion. We performed fully compressible, cavitating flow simulations to resolve the formation of the shock waves at cloud collapse – these are believed to be directly related to the formation of the damage. Good agreements were noticed between calculations and tests. Two high pressure peaks were found during one cavitation cycle. One relates to the cavitation collapse and the other one corresponds to the cavitation shed off, both contributing to a distinctive stepwise erosion damage growth pattern. Additional, more precise, simulations with much shorter time step were performed to investigate the processes of cavitation collapse and shedding off in more detail. There the importance of small cavitation structures which collapse independently of the main cloud was found.

The present work shows a great potential for future development of techniques for accurate predictions of cavitation erosion by numerical means only.

Key words: Cavitation, Erosion, Numerical simulation, Experiments

1 INTRODUCTION

The occurrence of cavitation, which is characterized by bubble inception, growth, shedding off and collapse, is many times unavoidable in hydraulic machinery. It generates where the local pressure drops below the fluid saturation pressure and disappears downstream when the pressure recovers. Severe problems are accompanied with the cavitation, inducing vibration and noise [1], deteriorating the hydrodynamic performance [2] and even eroding of the solid walls [3]. The last phenomenon – cavitation erosion - causes enormous economic loses in practical applications. Hence, more and more attention is paid on its research.

Since Rayleigh reported on the cavitation erosion issue on ship propellers in 1917, considerable progress has been made to discover its hydrodynamic mechanisms [4-7]. Two main mechanisms are usually discussed: the micro-jet and pressure shock wave. For the case of the micro-jet it is believed that the liquid jet penetrates the bubble as the surrounding pressure is imbalanced. The jet velocity can reach a magnitude order of 100 *m/s*, and when it impacts the solid wall enormous stresses that cause pit formation occur [8]. Crum photographically presented the micro-jet phenomenon by a high speed camera [9]. On the other hand the pressure shock wave approach, considers the bubbles to remain spherical during the collapse what, at the final stage causes a shock wave generation with a magnitude order of several MPa [10]. Fortes-Patella et al. [11] numerically studied the interaction between shock wave emitted by the implosions of a spherical bubble and material deformation. They concluded that the cavitation induced damage is directly related to the pressure shock wave and the characteristics of material. Subsequently, they proposed a so-called energy cascade theory. It postulated that potential energy contained in a macro cavitation cloud, considering the conservation of energy, would transfer into the radiation of acoustic pressure wave, which might be emitted either by spherical bubble or vortex collapse as well as micro jet. This assumption is also supported by Bark et al. [12-13].

Instead of analyzing the cause of the erosion formation, some other researchers discuss the correlation between cavitation structures and solid damage. Bensow et al. [14-15] investigated the sheet cavitation on a ship propeller by both experimental tests and numerical approach. It is noted that the sheet cavity seems to induce more severe erosion damage than the large cloud cavity, which implies that the micro cavity collapses are the main reason contributing to the damage. But Chen & Israelachvili [16] think it in another way, they suggested that the cavitation erosion tends to generate during the inception and growth, rather than collapse. However the work of Petkovsek & Dular [17] showed that no pits are produced during the formation of cavitation. In their experiment, the hydrodynamic cavitation evolution and cavitation induced erosion were synchronously recorded by two high speed cameras. It was found the damage only occurs at cavitation cloud collapse.

The rapidly development of computational power and numerical simulation technology, increase the potential and the accuracy of the methods for the prediction of cavitating flow and cavitation erosion power [18-21]. On the basis of the calculation, one can research the correlation of bubble structure and erosion quantitatively and qualitatively. Ochiai et al. [22] proposed a simulation method for predicting the cavitating flow around ClarkY 11.7% hydrofoil. The impact pressures on the solid surface were analyzed. Dular & Coutier-Delgosha [23] presented a prediction method of cavitation damage based on the micro-jet theory, by coupling a computational fluid dynamics (CFD) and the proposed erosion model. Analogously, Fortes-Patella et al. [11] obtained the cavity evolution through URANS model and predicted the cavitation-induced damage based on the energy cascade theory - a good agreement was noticed when compared with experimental observations. Schnerr et al. [24] developed an in-house conservative finite volume method CATUM (Cavitation Technische Universität München) to investigate the cavitating flow around a hydrofoil focusing the cavitation shock formation and propagation. An instantaneous local pressure peak of the order of 100bar was obtained on the hydrofoil surface, which was assumed to be responsible for the cavitation damages.

In the present paper we are comparing results of numerical simulations against experimental data obtained by Petkovsek & Dular [17]. We performed fully compressible, cavitating flow simulations to resolve the formation of the shock waves at cloud collapse – these are believed to be directly related to the formation of the damage. We have shown that two pressure peaks occur during one cavitation cycle, what consequently explains why the damage observed during the experiments occurs also at times other than at cavitation cloud collapse. Also the importance of small cavitation structures which collapse independently of the main cloud was confirmed.

The present work shows a great potential for future development of techniques for accurate predictions of cavitation erosion by numerical means only.

2 EXPERIMENT

The experiments were carried out in a cavitation loop test rig in the Laboratory for Water and Turbine Machines, University of Ljubljana. These are only briefly described here – for a more thorough description the reader should refer to [17].

A Venturi section, which has a converging angle of 18° and diverging angle of 8° was used. The size of the throat of the test section was 10×10mm^2. The geometry is shown in Fig. 1.

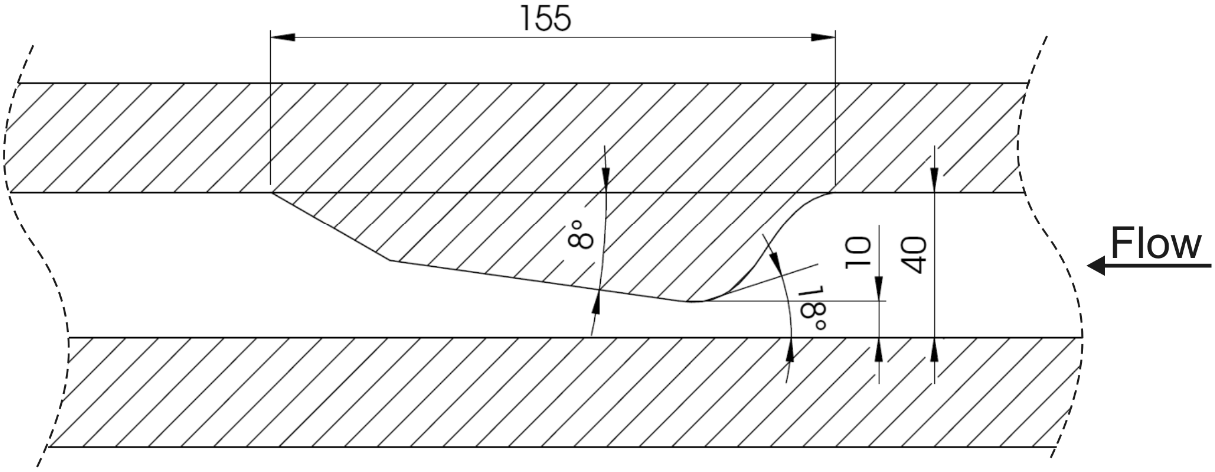

Fig.1: The Venturi geometry.

The idea of the experiment was to simultaneously record images of cavitation structures and cavitation erosion. The upper side of the foil is covered by vapour structures that obstruct the view, hence one needs to look at the foil from the bottom side to see the damage. Consequently the whole test section had to be made of transparent material and equally important the foil had to be thin enough so that the cavitation damage which occurs on the side exposed to cavitation was also visible on the other side. Furthermore the damage needs to occur very rapidly so that one is able to record it by high speed cameras - we have chosen 10 μm thick aluminum foil and attached it to a Venturi section by a transparent two sided adhesive tape with thickness of 50 μm. Using this approach a sufficient pitting can be obtained in a few seconds.

Two cameras were used in the experiment. For observation of the aluminum foil we used a high speed camera Fastec Imaging HiSpec4 2G mono which can capture images at 523 fps at 3Mpixel resolution. For capturing the cavitation structures from the side view we used high speed camera Motion Blitz EoSens mini 1 which can record at 506 fps at 1Mpixel resolution. For the present experiment the cameras were synchronized and recorded at 6000fps at a reduced resolution (Fig. 2).

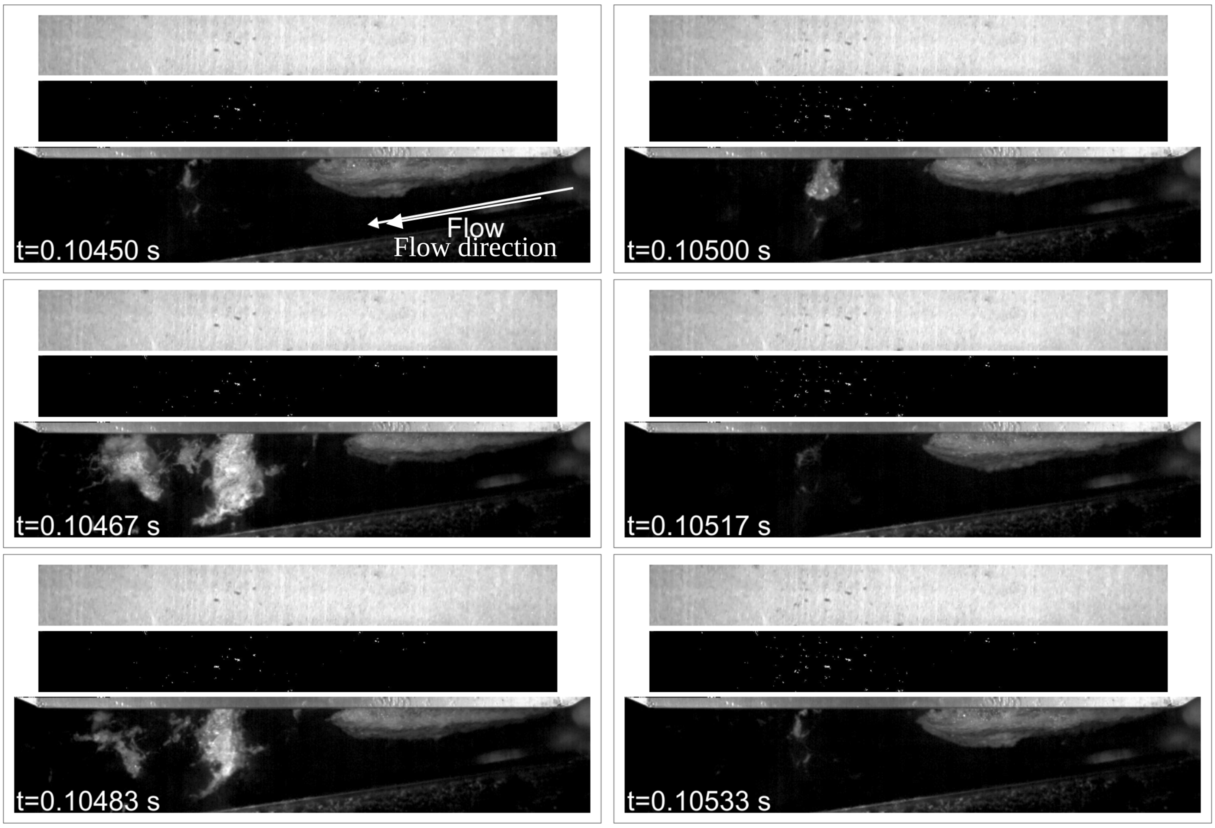

Fig. 2: Instantaneous image of the aluminum foil (top images), measured damage of the foil up to this instant (middle images) and instantaneous image of cavitation (bottom images) [17]. The flow is from the right to the left.

The flow direction in Fig.2 is from right to left. Cavitation cloud shedding begins with the cloud separation from the attached cavity. It then travels with the flow and collapses in a higher pressure region downstream. At the rear part of the attached cavity a back flow (re-entrant jet) forms that eventually cuts the cavity in two and causes a new separation of the cloud.

We can see that pits form immediately after the collapse of the cavitation cloud (in the present sequence we have two clouds that collapse at t=0.10500 s and 0.10517 s, respectively). It can also be seen that the region where most of the pitting occurs corresponds to the position of the cloud collapse. It is interesting to see that not a single pit forms but rather a cluster of them. We hypothesize that the shock wave from the cavitation cloud collapse interacted with several bubbles which were present in the vicinity of the wall (aluminum foil).

It also points to the idea of the cascade explanation of cavitation erosion process, which states that the damage occurrence is a consequence of a chain of events – for example cavitation cloud collapse, shock wave generation, spherical micro-bubble collapse or microject formation, and finally pit formation (Fortes-Patella et al. [11], Dular et al. [17]).

For evaluation we used an approach that combines several evaluation procedures used before (Dular et al. [25], Osterman & Dular [26] and Keil et al. [27]).

We evaluated the images in pairs – the image at the time t was subtracted from the image at time t+Δt, thus eliminating the surface and illumination imperfections. We employed the pit-count algorithm (Dular et al. [25]) which determines the pits from the darker regions in an image, while the brighter area is assumed to be undamaged surface - from each image pair we obtained the number and the area of newly appeared pits. The pit-count method gives a distribution of the number and the area of the pits and consequently, the distribution of the magnitude of cavitation erosion on the surface. We can also determine the distribution of the size of the pits. Since we were comparing pairs of two successive images we were also able to consider the possibility of pit overlapping.

3 MATHEMATICAL MODELS

3.1 The governing equations and homogenous flow model

The applied governing equations were based on the conservation form of the Reynolds averaged Navier-Stokes equations, including mass continuity (1), momentum equation (2) and energy equation (3):

$$\frac{\partial \rho_m}{\partial t}+\frac{\partial}{\partial x_i}(\rho_m \overline{u_i})=0 \tag{1}$$

$$\frac{\partial(\rho_m \overline{u_i})}{\partial t}+\frac{\partial(\rho_m \overline{u_i}\,\overline{u_j})}{\partial x_i}=-\frac{\partial p}{\partial x_i}+\frac{\partial}{\partial x_j}\left[(\mu_m+\mu_t)\left(\frac{\partial \overline{u_i}}{\partial x_j}+\frac{\partial \overline{u_j}}{\partial x_i}-\frac{2}{3}\delta_{ij}\frac{\partial \overline{u_k}}{\partial x_k}\right)\right] \tag{2}$$

$$\frac{\partial(\rho_m E)}{\partial t}+\nabla\cdot[\vec{u}(\rho_m E+p)]=\nabla\cdot(k_{eff}\nabla T) \tag{3}$$

The liquid phase and vapor phase are treated as a homogeneous mixture based on the volume of fraction. The mixture density and viscosity are defined as a function of vapor volume fraction:

$$\rho_m=\rho_v\alpha_v+\rho_l(1-\alpha_v) \tag{4}$$

$$\mu_m=\mu_v\alpha_v+\mu_l(1-\alpha_v) \tag{5}$$

where p is the pressure, ρ is the density, u is the velocity, μ and μ_t stand for the laminar viscosity and turbulent viscosity, δ_{ij} is the Kronecker delta function, $E=h-p/\rho_m+u^2/2$, h is the entropy, k_{eff} is the effective conductivity, α is the volume fraction. The subscripts m,l,v indicate the mixture, liquid and vapor, respectively.

3.2 Turbulence model

As known, the turbulence model plays a significant role in the prediction of cavitating flow. Since the standard k-ε model is over-estimating the eddy viscosity in the mixture region, it cannot effectively resolve the detachment of the cavity from solid surface and excessively attenuates the cavitation instability. However, the shedding motion and subsequent collapse are the primary reason causing cavitation erosion. Therefore, a modified Re-normalized group (RNG) k-ε model, proposed by Coutier-Delgosha et al. [28], was employed in this work. It can successfully reduce the eddy viscosity by defining the turbulent viscosity as:

$$\mu_t = f(\rho_m) C_\mu \frac{k^2}{\varepsilon} \tag{6}$$

$$f(\rho_m) = \rho_v + \frac{(\rho_m - \rho_v)^n}{(\rho_l - \rho_v)^{n-1}} \tag{7}$$

where the coefficient C_μ=0.09, identical with k-ε model, and the exponent n=10, recommended by Coutier-Delgosha et al. [28].

3.3 Cavitation model

The vapor generation and disappearance are controlled by a mass transport equation model (TEM) based on the vapor volume fraction, expressed as:

$$\frac{\partial \alpha_v}{\partial t} + \frac{\partial (\alpha_v u_j)}{\partial x_j} = \dot{m}^+ + \dot{m}^- \tag{8}$$

The source term $\dot{m}^+$ and $\dot{m}^-$ represent the mass rates of liquid evaporation and vapor condensation. In this paper, the Zwart-Gerber-Belamri model [29], deduced from the Rayleigh-Plesset equation, was applied, since it has, based on our previous experience, a precise cavitating prediction performance and a good convergence behavior. It is defined as:

$$\dot{m}^{+} = F_{vap}\frac{3r_{nuc}(1-\alpha_v)\rho_v}{R_B}\sqrt{\frac{2}{3}\frac{p_v - p}{\rho_l}}, \text{ if } p<p_v \tag{9}$$

$$\dot{m}^{-} = F_{cond}\frac{3\alpha_v\rho_v}{R_B}\sqrt{\frac{2}{3}\frac{p - p_v}{\rho_l}}, \text{if } p>p_v \tag{10}$$

where F_{vap} and F_{cond} are the empirical calibration coefficients of evaporation and condensation, respectively, r_{nuc} stands for the nucleation site volume fraction, R_B is the nucleation site radius. Vaporization is initiated at nucleation sites, which can be regarded as the non-condensible gases. p_v represents the water vaporization pressure. The recommended values of these coefficients are: F_{vap}=50, F_{cond}=0.01, $r_{nuc}=5\times10^{-4}$, $R_B=2\times10^{-6}$m and p_v=3574Pa.

As compressible approach was adopted [30]. The vapour obeyed the ideal gas law and the liquid density variation was described via Tait equation:

$$\rho_l = \rho_{ref}\sqrt[n]{\frac{p+B}{p_{ref}+B}} \tag{11}$$

where ρ_{ref} and p_{ref} denote the reference liquid density and pressure 200mm upstream of the venturi section. As for constant B and n, they are 300MPa and 7 for water, respectively.

4 MODELING

To get a better accuracy and convergence behavior, the structured hexahedral grid was generated to model the fluid computational domain, shown in Fig. 3. The model consists of two parts, the nozzle section and the Venturi section. The refinement was made near the Venturi surface, which is shown in more detail in Fig. 3 (bottom).

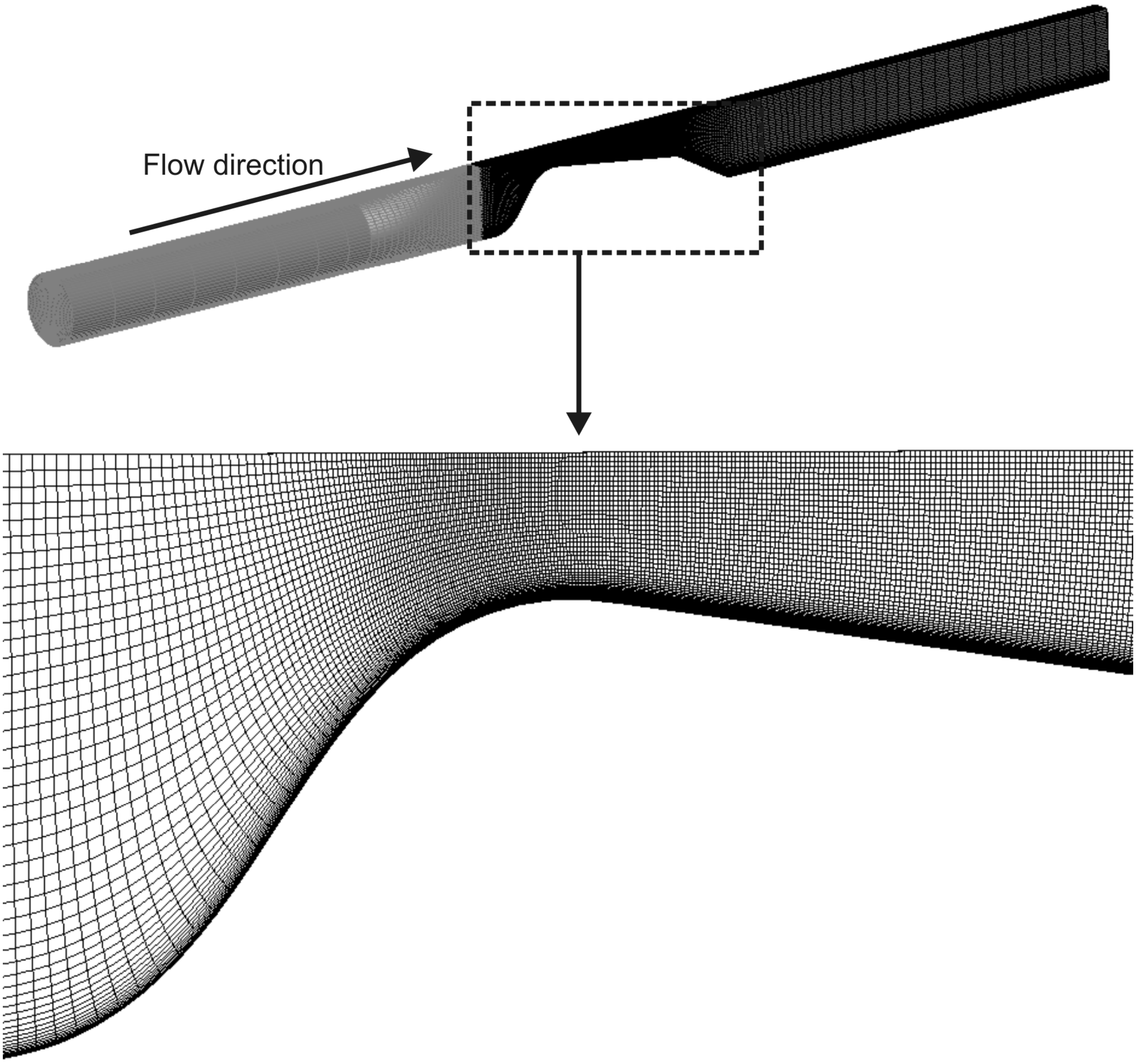

Fig.3: Computational domain. The flow is from the left to the right.

The grid independence test was conducted on the basis of three kinds of mesh density, among which the main difference is the grid distance from the Venturi surface to the first layer. The average cavity shedding frequency and cavity length and the average longest attached cavity length were selected as the criteria. To ensure the temporal accuracy and to avoid the initial transient of the simulation we calculated 20 shedding periods, then, the average frequency of the shedding was evaluated based on the last 10 periods, by means of monitoring the cavity evolution from inception and collapse and also the fluctuation of the absolute pressure near the collapse site. The same procedure was adopted for evaluation of the maximal attached cavity length. The results are shown in Tab. 1 (at cavitation number $\sigma = (p_{ref} - p_v)/(0.5\rho_l v^2)$ = 1.48 and the velocity at the Venturi throat v=24.7m/s - local Reynolds number *Re*=247,000). The detail numerical setups are described in section 4.1. One can see that the grid size has little influence on both the cavity length and the shedding frequency. Considering the calculation time and accuracy, the medium grid size was applied further on. The total number of the elements is about 0.5 million. The Y+ on the Venturi surface along with the chord length was in the order of 20.

Tab. 1: Grid independence test

	Grid number/10^6	Shedding frequency/Hz	Cavity length/mm
1	0.75	106.4	45.2
2	0.5	106.4	45.4
3	0.35	106.6	45.5

4.1 Simulation setup

The commercial CFD code "ANSYS-Fluent" was used to solve the URANS equations summarized above. A mass flow rate and static pressure boundary conditions are imposed on the inlet and outlet respectively, strictly following the experimental data. Meanwhile, the turbulent intensity at the inlet is set as 3%. A no-slip wall is applied on the venturi surface with standard wall function. The convergence criteria are all set to 1e-4. On the premise of ensuring the temporal accuracy, all the simulations were initiated by running the calculation under upwind scheme based on COUPLED algorithm for four shedding periods until a time-periodic solution has been reached, with a time step of 1.6×10^{-4} s, which corresponds to the experimental work, where the images were recorded at 6000 frames per second. Afterwards, the algorithm was changed to the second-order scheme and additionally, the time step was reduced to only 1.6×10^{-7} s to obtain a more precise resolution concerning to the cavity shedding off and collapse.

5 RESULTS

The cavity cloud shedding at σ=1.48 is first analyzed. The comparisons between computational results and experiments are made to validate the numerical simulations, as shown in Fig. 4. For the computational results, an isosurface of 10% vapor volume fractions are adopted, which relates best to the observations by naked eyes [28]. The $\Delta t=1.6\times10^{-4}$ s, which corresponds to the experimental image capturing frequency. A good agreement can be noted between simulation and experiment results. We can see that the attached cavity sheds off at around $t=t_0+20\Delta t$ both in simulation and in experiment. Subsequently, the cloud cavity collapse occurs approximately at $t=t_0+45\Delta t$. But still, some discrepancy can be observed after the shedding off. The inception of cavitation at the leading edge of the Venturi surface occurs earlier in the experiment – just after the cavity detachment at $t=t_0+20\Delta t$, in the calculation this occurs about $10\Delta t$ later. Nevertheless we believe that the numerical simulation is still reliable for the investigation of the potential energy during the cavitation collapse, since the collapse time matches well between the experiment and the simulation.

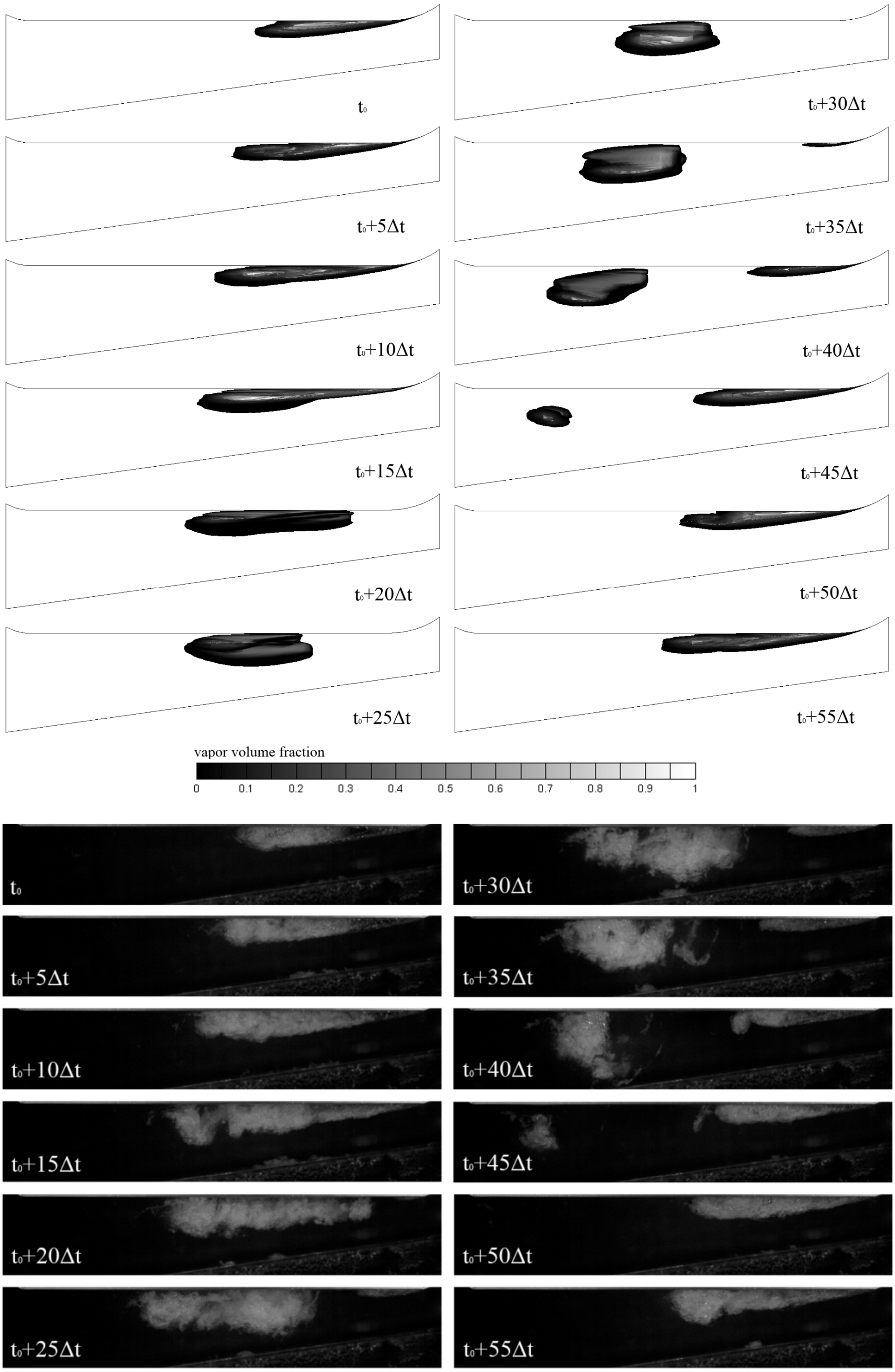

Fig. 4: Simulated (top) and observed (bottom) cavitation structure evolution, the flow direction is from right to left. $\sigma=1.48$ and $v=24.7m/s$.

For quantitative study of the relationship between the cavity evolution and the induced damage, the absolute pressure obtained from four monitor points on the Venturi surface are plotted together with the number of pits and integral damage area from the experiment [11], as a function of time. The locations of the monitors are shown in Fig. 5. As illustrated in the figure, point A is located near the throat of the Venturi (5 mm downstream), from where we can investigate whether there is high potential energy produced during cavity shedding. As for monitor D, it is located near the region where the bubble cloud collapse takes place (65 mm downstream of the Ventuiri thorat), so that the pressure shock wave emitted by it can be recorded in detail. Monitors B and C are placed between A and D (22 mm and 48 mm downstream of the Venturi throat, respectively).

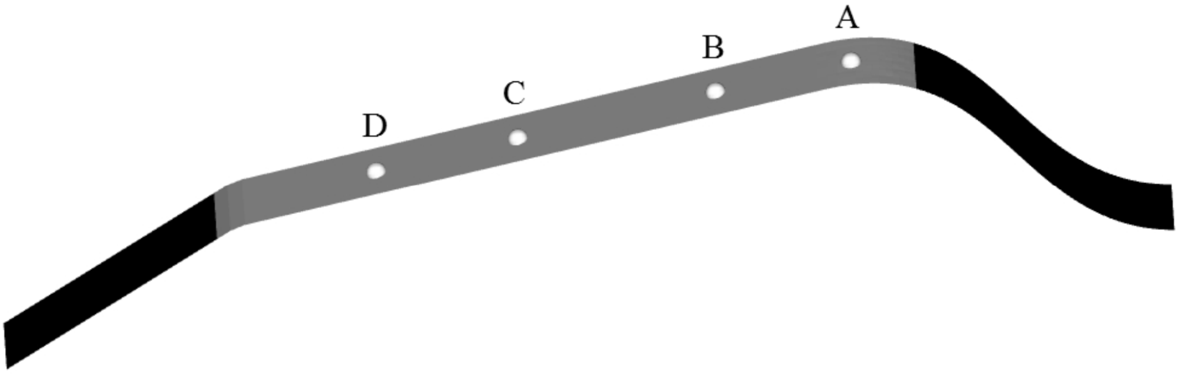

Fig. 5: Monitor points (A lies 5mm, B 22 mm, C 48mm and D 65 mm downstream of the throat of the Venturi).

The diagram in Fig. 6 shows the absolute pressure obtained at four monitor points and the number of pits and integral damage area from the experiment [11]. The selected observation period extends over 0.05s (from 0.15 to 0.20 s after the start of the experiment) and includes about six shedding cycles. The simulation data adopted here are obtained with a time step of 1.6×10^{-4} s. The exact cavity collapse times from the experiment are presented as vertical dash-dot lines in this diagram.

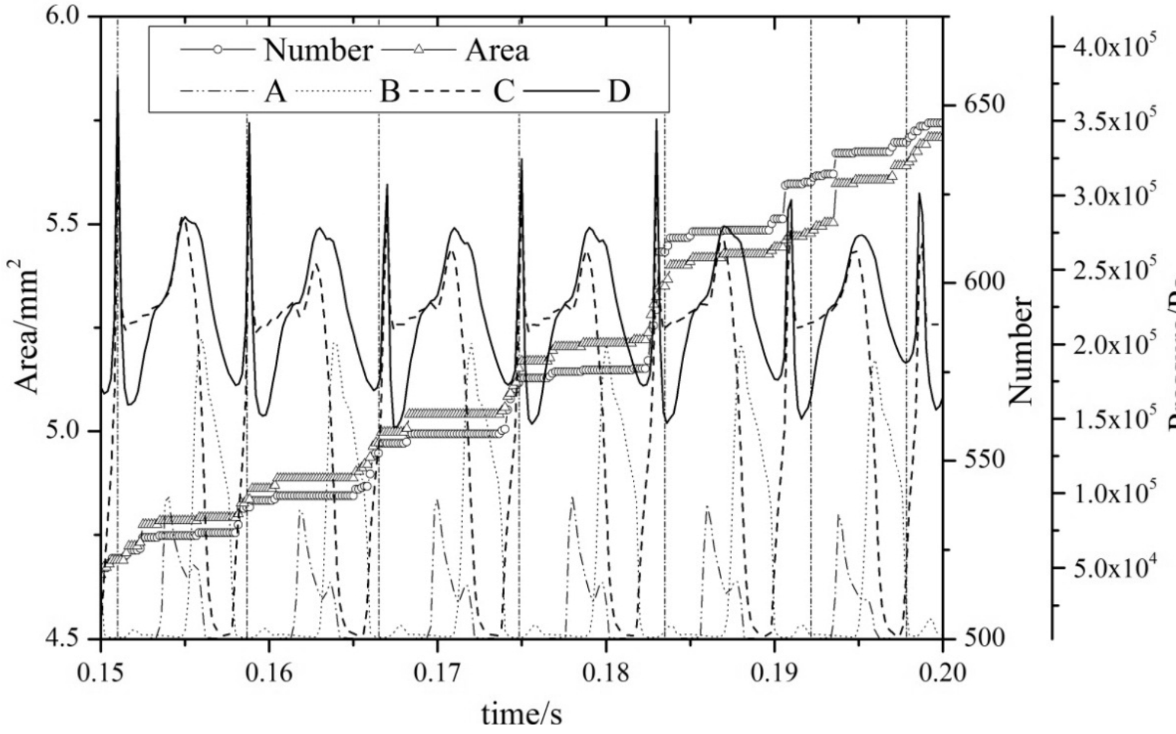

Fig. 6: Number of pits, integral damage extent and absolute pressure at the monitor points A, B, C, and D (see Fig. 5 for positions) as a function of time. At cavitation number σ=1.48 and velocity at the Venturi throat v=24.7m/s, Reynolds number Re=247000.

It can be seen that with the time progressing, the number of the pits and the damaged area are not increasing at a constant pace. A considerable damage occurs only during a period of cloud collapse. More precisely, it can be noticed that some the damage is also generated just before the main cavitation cloud disappears. The reason is that the cavity collapse is not instantaneous - some tiny bubbles collapse before the main cavity collapse, which can be also seen in Fig. 4 (bottom) between $t= t_0+35\Delta t$ and $t= t_0+45\Delta t$.

As for the simulation, we can observe that there are two high pressure peaks in one cycle, especially at points C and D. The higher peak corresponds to the cloud collapse, while the other one is related to the moment of cavity shedding off. It can be seen that the pressures recorded at monitor D are the highest and reach up to 3.5×10^5 Pa. Considerable pressure increase from the cloud collapse is also seen by monitor C, while monitors A and B, which are further away from the collapse region, notice only a small disturbance in the pressure.

It is fair to claim that the numerical simulation has pronounced agreement with the experiment - the high pressure shockwaves, which are generated just after the cavity collapse, contribute to the growth of the pit number and the damage area. Also one can see that in the experiment some damage occurs in the period between the collapses. On the basis of the simulation we can conclude that this occurs during the breaking off of the cloud, when some individual bubbles collapse without merging into a large cloud. A similar conclusion can also be reached from recently published experimental work of Bark and Bensow [12]. And also there are some damages generated from the attached part of the cavity. At this instant the simulation shows a secondary, smaller, pressure increase which is best seen from monitors A and B as they lie in the region of cavitation cloud separation. To support this claim, the simulated instantaneous pressure on the Venturi surface, the pits on the aluminum foil and the cavity structures are analyzed together in Fig. 7.

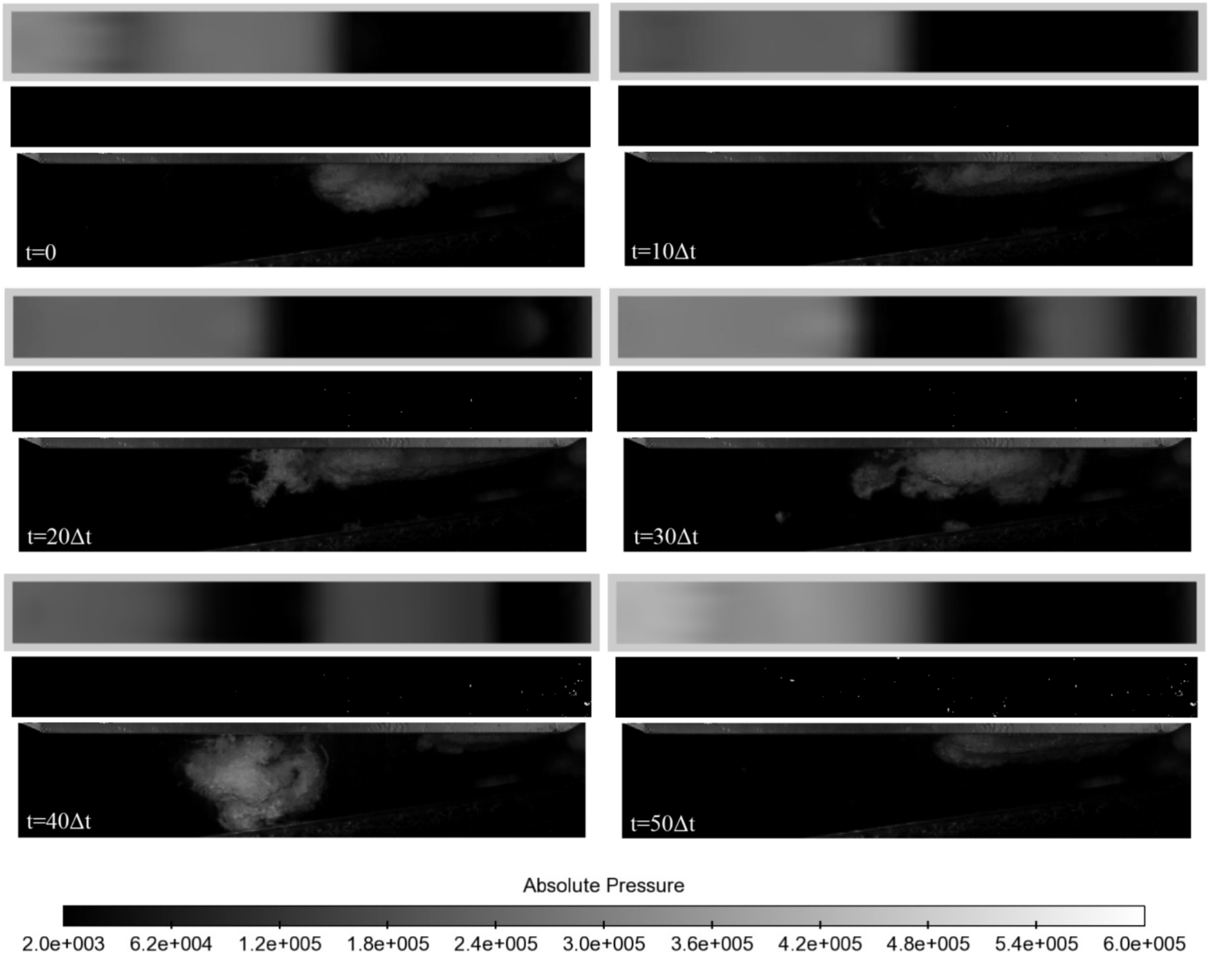

Fig. 7: Instantaneous simulated absolute pressure on the Venturi surface (top images), measured damage of the foil (middle images) and instantaneous image of cavitation (bottom images). $\sigma=1.48$ *and* $v=24.7m/s$. *The flow direction is from right to left.*

A full shedding cycle is presented in Fig. 7. The sequence starts exactly after the previous cavitation cloud disappears. Of course, the absolute pressure on the foil (the upper image) is low where cavitation exists. And also, the length of the low pressure region matches the cavitation length well - even for the detached cloud cavitation (at t=40Δt).

As for the damage on the foil (the middle image), we can see that during the growth of the attached cavitation, form t=0 to t=20Δt, only a few pits (seen as white dots) occur. They might be caused by the tiny bubbles at the rear part of the cavitation, where the cavitation is very unstable. At t=30Δt, the cavitation starts shedding off and a new attached cavitation forms near the throat of the Venturi a few micro seconds after. It can be noticed that during the period from t=30Δt to t=40Δt, a numbers of pits appear in the vicinity of the throat – conveniently the simulation predicts a high pressure peak in this region and time. This supports our claim that the shedding off of the cavitation can cause the erosion damage.

Finally, at the cavitation collapse step from t=40Δt to 50Δt, one can again observe an increase of the pressure and the correspondingly a large amount of pits appearing in the vicinity of the cloud collapse site. One can conclude that the main erosion damage results from the cavitation cloud collapse while some is also produces during the shedding off the cloud.

More precisely simulations with a much smaller time step 1.6×10^{-7} s were conducted to investigate the correlation between damage appearance, the cavitation cloud collapse and the shedding of the cloud. Figure 8 shows the absolute pressure at monitor D, obtained by simulations under two different time steps. The onset point of the simulation is just before the cavitation collapse, corresponding to t=0.1826s in Fig. 7.

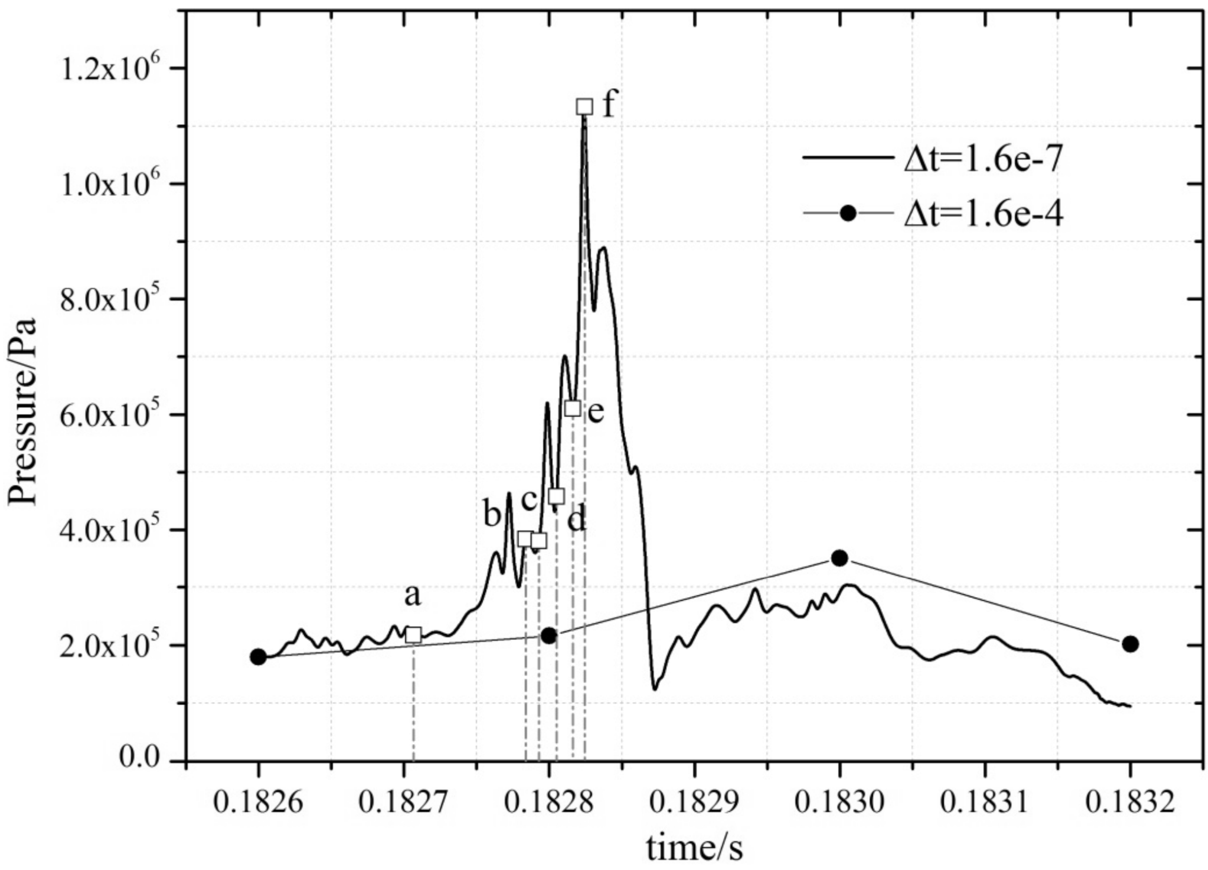

Fig.8: Comparison of absolute pressure between different time step simulations at Monitor D when cavitation cloud collapsing. σ=1.48 and v=24.7m/s.

As can be seen, with much smaller time step, that the prediction of the potential energy emitted by the cavitation collapse is more rigorous. There are several pressure fluctuations before it reaches the highest point, which implies that the cavity collapse is not instantaneous. The highest pressure predicted by the smaller time step 1.6×10^{-7}s is approximately 1.1×10^{6} Pa, while the value of only 3.5×10^{5} Pa was obtained from the simulation with $\Delta t=1.6\times10^{-4}$ s.

To understand the details of the collapse evolution, six instants are chosen to present the absolute pressure on the Venturi surface together with the cavitation, Fig. 9. The white dot in the graph represents the monitor D.

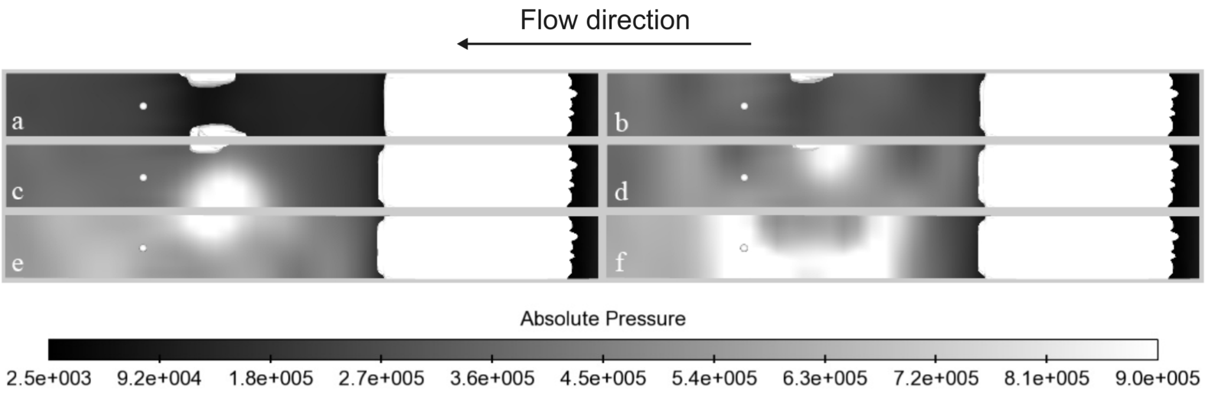

Fig. 9: Absolute pressure at the Venturi surface at times a to f during cavitation cloud collapse. σ=1.48 and v=24.7m/s. The flow direction is from right to left.

In the image a, there are two big bubbles clouds close to the side wall of the venturi section and the pressure is low at this moment. The instant of the image b is chosen just after one of the bubble clouds below disappear. One can see that the shock wave has not arrived at the venturi surface yet - this is why the pressure on the surface is still low. Several micro seconds later, the collapse shock wave impacts the surface (image c), where we can see a concentrated region of a very high pressure. Image d, illustrates that during the collapse of the other bubble cloud, some tiny bubbles around it also generate pressure shock waves as they collapse. In images e and f, one can see how the shock wave propagated through the region and after it is emitted at the origin of cloud collapse.

Identically, Fig.10 presents the absolute pressure in point A. It is clear that with a smaller time step, the simulation can predict much more detail of the shedding phenomenon.

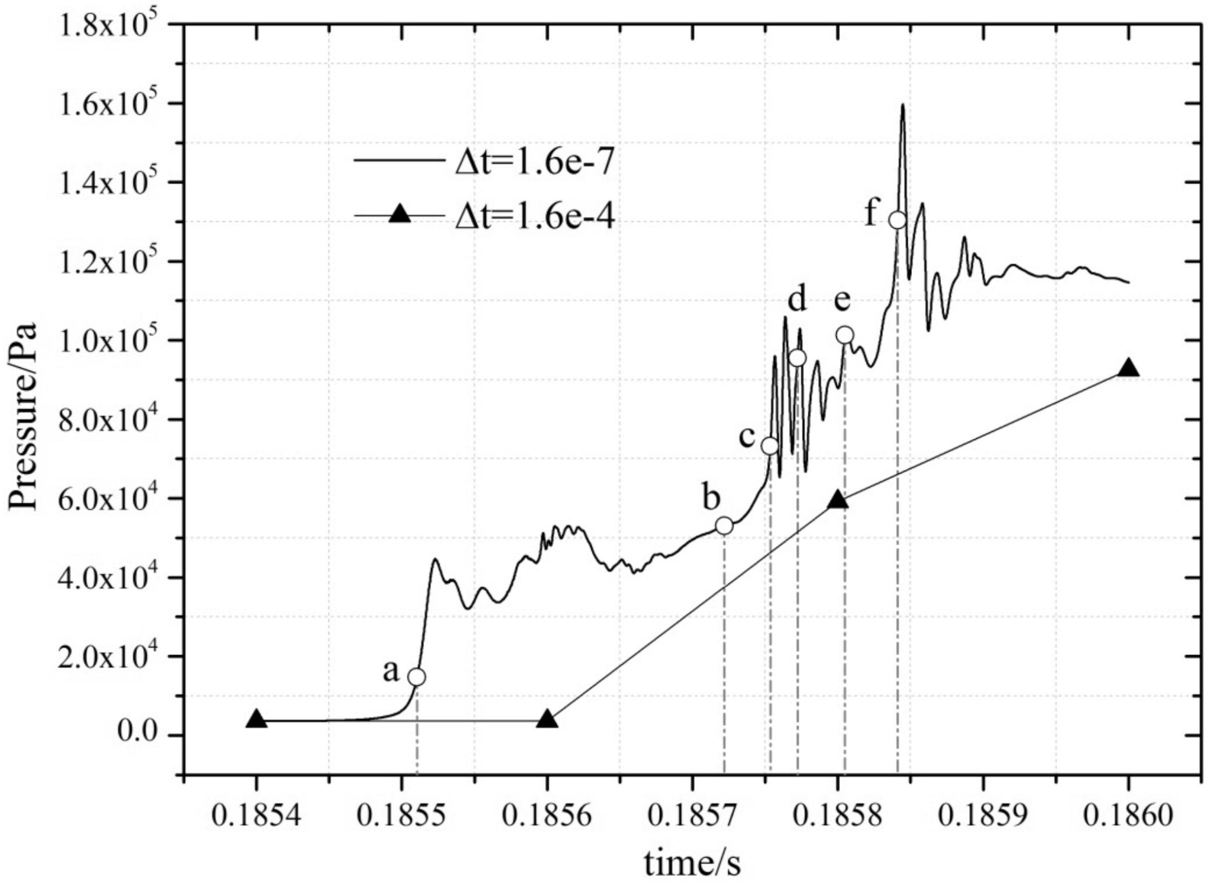

Fig.10: Comparison of absolute pressure between different time step simulations at Monitor A at cavitation shedding off. σ=1.48 and v=24.7m/s.

From t=0.1854 s to t=0.18585 s, the pressure during the shedding keeps on increasing, reaching a peak of 1.6×10^5 Pa. After the detachment, the less detailed simulation predicts the pressure continues to rise, while in the more detailed one it settles and remains at a certain level.

Again we plot six instants to present the absolute pressure on the Venturi surface together with the cavitation during the shedding process (Fig.11). The gray dot in the images represents the monitor A.

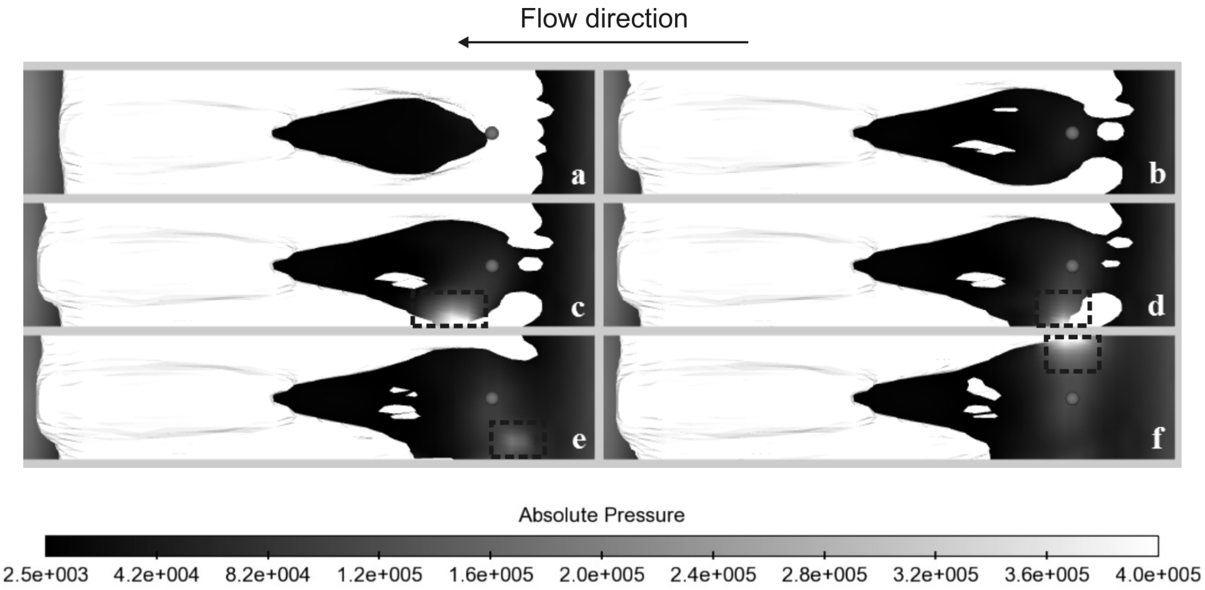

Fig. 11: Absolute pressure on Venturi surface at times a to f during cavitation shedding process. σ=1.48 and v=24.7m/s. The flow direction is from right to left.

In image a, we can see that the cavitation is beginning to shed, but no high pressure region can be seen yet. A pressure peak first appears after the cavitation breaks off (image c) – in a very small region (noted by a dashed square). After breaking off, a small bubble remains at the leading edge (image d). When it vanishes, some high pressure shock waves are emitted from time c to time e, which can be more obviously seen in Fig. 10. At time f, the cavitation begins to shed off on the other side of the channel, but there is no break off, so only one high pressure peak appears at this moment. This shows how and when the pressure peak is created during the shedding process, which eventually leads to a, previously hard to explain, damage near the throat of the Venturi.

7 CONCLUSIONS

In this paper, a compressible approach to simulate cavitating flow in a Venturi section was performed with two different time steps. The results were firstly validated against visualization experiments, and then some new insights into the formation of damage were drawn from the results. The conclusions can be given in several points:

(1) From the erosion tests, we see that most of the damages occurs at the point of cavitation cloud collapse. Yet it was also reported [11] that some damage occurs just before and after the cavitation cloud collapse, and even during the shedding process. The simulation results, obtained with a larger time step of 1.6×10^{-4} s, are in a good agreement with the visualization experiments. Absolute pressure on the Venturi surface as a function of time at four monitor points were compared with the erosion measurements. We observed two pressure peaks in one cycle. The higher one relates to the cloud collapse and the other corresponds to the shedding off the cloud from the attached part of the cavity, what partially explained a not rigorously stepwise trend of the damage occurrence.

(2) Instantaneous images of the absolute pressure on the Venturi surface, measured erosion damage of the foil and the instantaneous image of cavitation were analyzed simultaneously. It was found that the main damage occur at the cavitation cloud collapse, as a clear result of a very high pressure wave which is emitted at that instant. Besides this we were able to conclude that a somewhat less pronounced pressure peak occurs during the cloud shedding process – and that this also contributes to some cavitation erosion pits. There are also some indications that an almost negligible number of pits is generated during the growth of the attached cavitation.

(3) Finally, based on a more time resolved simulation (time step length was only 1.6×10^{-7} s), we observed instabilities during the collapse and the shedding of cavitation cloud. We were able to show that the cavitation collapse is not instantaneous and coherent – many tiny bubbles collapse prior and after the main clouds collapse and these also considerably contribute to the erosive energy potential of cavitating flow.

ACKNOWLEDGEMENTS

The work was performed in the scope of the project “Cavitation in Thermosensible Fluids” finantially supported by the European Space Agency (ESA). J. Wang would like to thank the State Scholorship Fund for the financial support by the China Scholarship Council which enabled him the stay at University of Ljubljana, during which this work was performed. And also, J. Wang would like to thank the support by the National Natural Science Foundation of China (51239005, 51309120, 51109095, 51179075); The Scientific Research Innovation Program in Colleges and Universities of Jiangsu Province (Grant No. CXLX12_0640).

Nomenclature

B = constant number in Tait equation

E = energy

F_{vap} = coefficient of evaporation

F_{cond} = coefficient condensation

h = entropy

k_{eff} = effective conductivity

$\dot{m}^{+}$ = mass rates of liquid evaporation

$\dot{m}^{-}$ = mass rate of vapor condensation

n = constant number in density corrected equation and Tait equation

p = local mixture pressure

p_{ref} = reference pressure

p_v = water vaporization pressure

R_B = nucleation site radius

r_{nuc} = nucleation site volume fraction

$u_{i,j,k}$ = velocity of the mixture

t = instantaneous time

Δt = simulation time step

t_0 = chosen simulation initial time

α = vapor volume fraction

$\rho_{m,l,v}$ = mixture, liquid, vapor density

μ = laminar viscosity

μ_t = turbulent viscosity

δ_{ij} = Kronecker delta function

ρ_{ref} = reference liquid density and

σ = cavitation number

References

[1] Yamada, H., and Uchiumi, M., 2008, “A Case Study of fluid-Dynamic Vibrations of Rocket Turbopumps,” Turbomachinery, 36 (2), pp.3–9.

[2] Liu, H. L., Wang, J., Wang, Y., Zhang, H., and Huang, H., 2014. “Influence of the Empirical Coefficients of Cavitation Model on Predicting Cavitating Flow in the Centrifugal Pump,” International Journal of Naval Architecture and Ocean Engineering, 6(1), pp.119-131.

[3] Dular, M., Bachert, B., Stoffel, B., and Širok, B., 2004. “Relationship between Cavitation

Structures and Cavitation Damage," Wear, 257(11), pp.1176-1184.

[4] Kato, H., Konno, A., Maeda, M., and Yamaguchi, H., 1996, "Possibility of Quantitative Prediction of Cavitation Erosion without Model Test," ASME J. Fluids Eng., 118(3), pp. 582–588.

[5] Berchiche, N., Franc, J. P., and Michel, J. M., 2002, "A Cavitation Erosion Model for Ductile Materials," ASME J. Fluids Eng., 124(3), pp.601–606.

[6] Franc, J. P., Karimi, A., Chahine, G. L., and Riondet, M. 2011, "Impact Load Measurements in an Erosive Cavitating Flow," ASME J. Fluids Eng., 133(12), pp.121301.

[7] Franc, J. P, 2009, "Incubation Time and Cavitation Erosion Rate of Work-Hardening Materials," ASME J. Fluids Eng., 131(2), 021303.

[8] Franc, J. P., Riondet, M., Karimi, A., and Chahine, G. L., 2012. "Material and Velocity Effects on Cavitation Erosion Pitting," Wear, 274, pp.248-259.

[9] Crum, L. A., 1995. "Comments on the Evolving Field of Sonochemistry by A Cavitation Physicist," Ultrasonics Sonochemistry, 2(2), pp.147-152.

[10] Wang, Y. C., and Brennen, C. E., 1994. "Shock Wave Development in the Collapse of A Cloud of Bubbles," ASME. American Society of Mechanical Engineers, 194, pp.15-19.

[11] Patella, R. F., Archer, A., and Flageul C., 2012. "Numerical and Experimental Investigations on Cavitation Erosion," IOP Conference Series: Earth and Environmental Science, 15(2):022013.

[12] Bark, G., and Bensow, R. E., 2014. "Hydrodynamic Processes Controlling Cavitation Erosion," in Advanced Experimental and Numerical Techniques for Cavitation Erosion

Prediction, Kim, K.-H., Chahine, G., Franc, J.-P., and Karimi, A. Edts., Springer.

[13] Bark, G., and Bensow, R. E., 2013. “Hydrodynamic Mechanisms Controlling Cavitation Erosion,” International Shipbuilding Progress, 60(1), pp.345-374.

[14] Bensow, R., Bark, G., and Lu, N. X., 2012. “Hydrodynamic Mechanisms in Cavitation Erosion,” Proc. 8th Int. Sym. Cavitation, CAV2012, Singapore.

[15] Bensow, R. E., and Bark, G., 2010, “Implicit LES Predictions of the Cavitating Flow on A Propeller,” ASME J. Fluids Eng., 132, p. 041302.

[16] Chen, Y. L., and Israelachvili, J., 1991. “New Mechanism of Cavitation Damage,” Science, 252, pp.1157-1160.

[17] Petkovšek, M., and Dular, M., 2013. “Simultaneous Observation of Cavitation Structures and Cavitation Erosion,” Wear, 300(1), pp.55-64.

[18] Wang, Y. C., and Brennen, C. E., 1999, “Numerical Computation of Shock Waves in a Spherical Cloud of Cavitation Bubbles,” ASME J. Fluids Eng.,121(4), pp.872–880.

[19] Li, Z. R., Pourquie, M., and Terwisga, T., V., 2014, “Assessment of Cavitation Erosion With a URANS Method.” ASME J. Fluids Eng., 136(4), pp.041101.

[20] Luo, X., Ji, B., Peng, X., Xu, H., and Nishi, M., 2012, “Numerical Simulation of Cavity Shedding from a Three-Dimensional Twisted Hydrofoil and Induced Pressure Fluctuation by Large-Eddy Simulation,” ASME J. Fluids Eng., 134(4), pp.041202.

[21] Huang, B., Young, Y. L., Wang, G., and Shyy, W., 2013, “Combined Experimental and Computational Investigation of Unsteady Structure of Sheet/Cloud Cavitation,” ASME J. Fluids Eng., 135(7), pp.071301.

[22] Ochiai, N., Iga, Y., Nohmi, M., and Ikohagi, T., 2009. “Numerical Prediction of

Cavitation Erosion in Cavitating Flow," Proc. 7th Int. Sym. Cavitation, CAV2009, USA.

[23] Dular, M., and Coutier-Delgosha, O., 2009, "Numerical Modelling of Cavitation Erosion," Int. J. Numer. Meth. Fluids, 61(12), pp. 1388–1410.

[24] Schnerr, G. H., Sezal, I. H., and Schmidt, S. J., 2008, "Numerical Investigation of Three-Dimensional Cloud Cavitation with Special Emphasis on Collapse Induced Shock Dynamics," Physics of Fluids, 20(4), 040703.

[25] Dular, M., Bachert, B., Stoffel, B., and Sirok, B., 2004. "Relationship between Cavitation Structures and Cavitation Damage," Wear 257, pp. 1176–1184.

[26] Dular, M., and Osterman, A., 2008. "Pit Clustering in Cavitation Erosion," Wear, 265(5), pp.811-820.

[27] T. Keil, P. F. Pelz, U. Cordes, G. Ludwig, 2011. "Cloud Cavitation and Cavitation Erosion in Convergent Divergent Nozzle," WIMRC 3rd International Cavitation Forum 2011 University of Warwick, UK.

[28] Coutier-Delgosha, O., Fortes-Patella, R., and Reboud, J. L., 2003. "Evaluation of the Turbulence Model Influence on the Numerical Simulations of Unsteady Cavitation," Journal of Fluids Engineering, 125(1), pp. 38－45.

[29] Zwart, P., Gerber, A. G., and Belamri, T., 2004. "A Two-Phase Model for Predicting Cavitation Dynamics," Proceedings of ICMF2004 International Conference on Multiphase Flow, Yokohama, Japan.

[30] Dular, M., Bachert, R., Stoffel, B., and Širok, B., 2005. "Experimental Evaluation of Numerical Simulation of Cavitating Flow around Hydrofoil," European Journal of Mechanics-B/Fluids, 24(4), pp. 522-538.